metals

MDPI

Article

Potentiostatic Dealloying Fabrication and Electrochemical Actuation Performance of Bulk Nanoporous Palladium

Fuquan Tan [1], Bin Yu [1], Qingguo Bai [2,*] and Zhonghua Zhang [1,*]

[1] Key Laboratory for Liquid-Solid Structural Evolution and Processing of Materials (Ministry of Education), School of Materials Science and Engineering, Shandong University, Jingshi Road 17923, Jinan 250061, China
[2] School of Applied Physics and Materials, Wuyi University, Dongcheng Village 22, Jiangmen 529020, China
* Correspondence: qingguo.bai@asu.edu (Q.B.); zh_zhang@sdu.edu.cn (Z.Z.)

Abstract: Metallic actuators increasingly exhibit superiority over conventional actuators (such as piezoelectric ceramics) via low energy consumption and large strain amplitude. Large strain amplitude and high strain energy density (or work density) are required for an actuator with excellent comprehensive performance. Herein, we fabricated bulk nanoporous Pd (np-Pd) with a dense nanoporous structure by two-step potentiostatic dealloying of as-annealed Ni–Pd alloy with chemical corrosion resistance, and investigated the dealloying behaviors as well as electrochemical actuation performance. A visible current density oscillation occurred during dealloying, which is related to formation/dissolution of the passivating film. Additionally, since the dense and continuous ligaments establish a good network connectivity for large strain response, the np-Pd achieves a strain amplitude of up to 3.74% and high strain energy density, which stands out among many actuator materials (e.g., np-AuPt, np-Ni, and np-AlNiCu). Our study provides a useful guidance for fabricating metallic actuators with excellent comprehensive performance.

Keywords: electrochemical actuation; potentiostatic dealloying; nanoporous Pd; strain amplitude; strain energy density

check for updates

Citation: Tan, F.; Yu, B.; Bai, Q.; Zhang, Z. Potentiostatic Dealloying Fabrication and Electrochemical Actuation Performance of Bulk Nanoporous Palladium. *Metals* **2022**, *12*, 2153. https://doi.org/10.3390/met12122153

Academic Editor: Jeff Th. M. De Hosson

Received: 15 November 2022
Accepted: 13 December 2022
Published: 15 December 2022

Publisher's Note: MDPI stays neutral with regard to jurisdictional claims in published maps and institutional affiliations.

Copyright: © 2022 by the authors. Licensee MDPI, Basel, Switzerland. This article is an open access article distributed under the terms and conditions of the Creative Commons Attribution (CC BY) license (https://creativecommons.org/licenses/by/4.0/).

1. Introduction

In recent decades, nanoporous metals (np-metals) have attracted intense research interests due to their bi-continuous ligament-channel network structure. The unique architecture is enriched with a large number of active surface defects, facilitating charge transfer reactions during electrochemical processes, and the interconnected metal ligament framework provides excellent conditions for high electrical conductivity [1]. Therefore, np-metals have a wide range of applications in many fields, such as catalysis [2,3], sensing [4], energy storage [5], and actuation [6]. Among them, electrochemical metallic actuators have gradually been receiving more and more attention in the past two decades because of the salient advantages of low energy consumption and large strain amplitude compared with piezoelectric ceramics, as well as higher strength than that of conducting polymer [7]. Electrochemical metallic actuators rely on electrical energy consumption to generate dimensional changes. To achieve desirable comprehensive actuation performance, in addition to large strains, the high strain energy density (or work density) beneficial for the device to work efficiently in the case of space (or mass) limitations [8] is also a critical element to be considered.

At present, electrochemical metallic actuator materials can typically be derived from np-metals prepared by dealloying (e.g., np-Pt [9,10], and np-Au [11,12], np-Ni [13,14], np-NiMn [15], np-Pd [16,17], np-Cu [18,19], np-AlNiCu [20]) or the composites of np-metals and polymer (e.g., the hybrid of np-Au/polypyrrole [21–23] or np-Au/polyaniline [24]). Both chemical and electrochemical dealloying are common methods for fabricating np-metals [1,5]. The latter especially can achieve a precise regulation for the morphology,

composition and porosity of as-dealloyed samples via exclusively changing the applied potential/current [12,25–27]. Moreover, the electrolyte used for electrochemical dealloying has a wide range of selections and plays an important role in the dealloying potential [28–31]. Solutions that are almost invalid for a given alloy under chemical dealloying can work under electrochemical conditions, such as electrochemical dealloying of Al-based alloys in NaCl solution [28,32] or Ag-Au alloys in $AgNO_3$ solution [33]. Therefore, electrochemical methods may be available for dealloying some alloys with corrosion resistance.

Herein, we explored a two-step potentiostatic dealloying method to dealloy a Ni–Pd alloy with chemical corrosion resistance. During dealloying, the current density oscillation is considered to be associated with the formation/dissolution of the passivating film. After dealloying, the Ni element was successfully removed to obtain the bulk np-Pd. Noteworthily, our np-Pd possesses a dense nanoporous structure instead of a hierarchically porous structure such as many reported electrochemical metallic nanoporous actuators [13,14,16–20]. Tightly intertwined ligaments of the bulk np-Pd establish a good network connectivity, thereby achieving a large strain amplitude of up to 3.74%, which is superior to those of many reported actuator materials, such as np-Ni [13], np-Pd [16] and np-AlNiCu [20]. Furthermore, the volume- and mass-specific strain energy density is at a high level, significantly better than those of np-AuPt [7]. Therefore, our results demonstrate that the bulk np-Pd with the dense nanoporous structure has excellent electrochemical actuation performance.

2. Experimental Mehods

A $Ni_{80}Pd_{20}$ alloy ingot was obtained by high-frequency induction heating of Ni particles (99.9 wt.%) and Pd sheets (99.99 wt.%) in a sealed quartz tube under an argon atmosphere. The ingot was cut into cubes of size $1 \times 1 \times 1$ mm^3 after annealing treatment at 900 °C for 12 h for two times. The electrochemical dealloying was carried out in a three-electrode system, and the potential stimuli were provided by a potentiostat (CHI 760E). The as-annealed Ni–Pd alloy cubes, Ag/AgCl electrode, and a graphite rod served as the working electrode (WE), reference electrode (RE), and counter electrode (CE), respectively. The as-annealed alloy cubes were dealloyed under two-step potentiostatic control (from 0.5 to 0.6 V vs. Ag/AgCl) in a 0.5 M H_2SO_4 solution. The scenario where the current density fell abruptly indicated the end of dealloying at the corresponding potential [28].

The microstructures/phases of the Ni–Pd alloy were characterized by the back-scattered electron (BSE, Daejeon, Korea) imaging mode of scanning electron microscope (SEM, COXEM EM-30, Daejeon, Korea) equipped with an energy-dispersive X-ray spectrometer (EDS, Daejeon, Korea). EDS was undertaken to investigate the chemical compositions and elemental distributions of both the Ni-Pd alloys and as-dealloyed samples. The morphologies of the as-dealloyed samples were examined by field-emission SEM (JSM-7610F, Japan) and transmission electron microscope (TEM, Tecnai F20, United States). The final ligament size was determined by the average of 300 ligament diameters. An X-ray diffractometer (XRD, XD-3, Beijing Purkinje General Instrument Co., Ltd., Beijing, China) with Cu Kα radiation was used to analyze the phase constitutions of the Ni-Pd alloy and as-dealloyed samples.

The electrochemical actuation measurements were performed in the three-electrode system with a 0.7 M NaF solution, and the potentiostat provided the potential stimuli. The schematic illustration of the actuation device is shown in Figure 1. The saturated calomel electrode (SCE), and the Pt sheet acted as the RE and CE, respectively. The bulk np-Pd sample immersed into the NaF solution was placed onto a gold substrate connected to the WE of the potentiostat via a gold wire. A pushrod contacted the top surface of the sample as well as the bottom of the displacement sensor (Solartron, DP/1/S). When the potential was applied, the sample would generate a volume change, and the vertical displacement of the sample was converted by the sensor into a numeric signal to the computer.

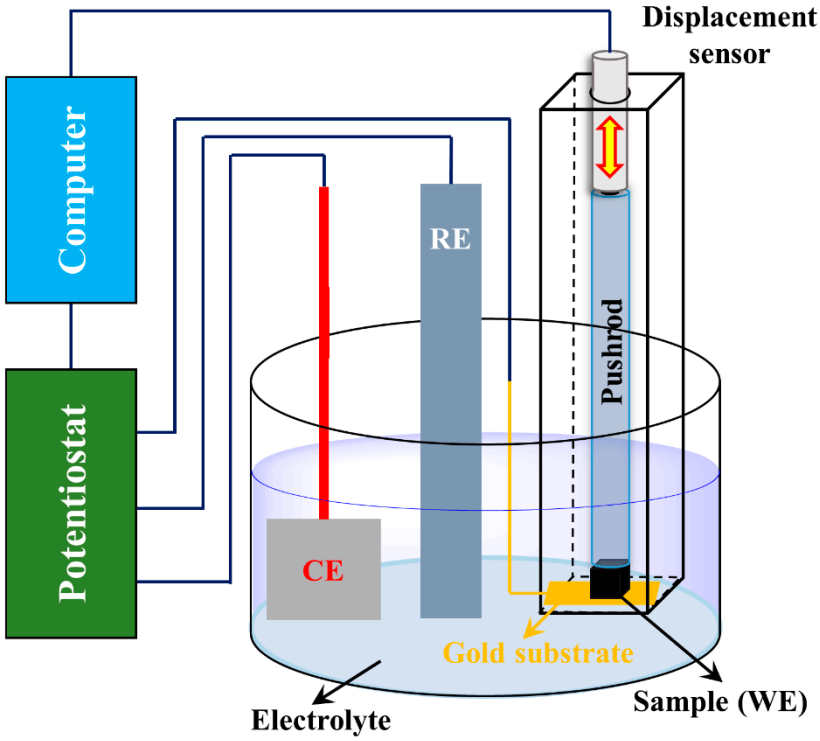

Figure 1. Schematic illustration of the actuation device with three electrodes.

3. Results and Discussion

According to the EDS element analysis (Figure 2a), the chemical compositions of the as-annealed alloy are consistent with the nominal values of $Ni_{80}Pd_{20}$. Furthermore, the XRD pattern (Figure 2b) of the as-annealed alloy reveals only one group of diffraction peaks which deviate slightly from those of the face-centered cubic (fcc) Ni (PDF # 04-0850), although the alloy consists of two solid–solution phases with extremely close chemical compositions (Figure 3).

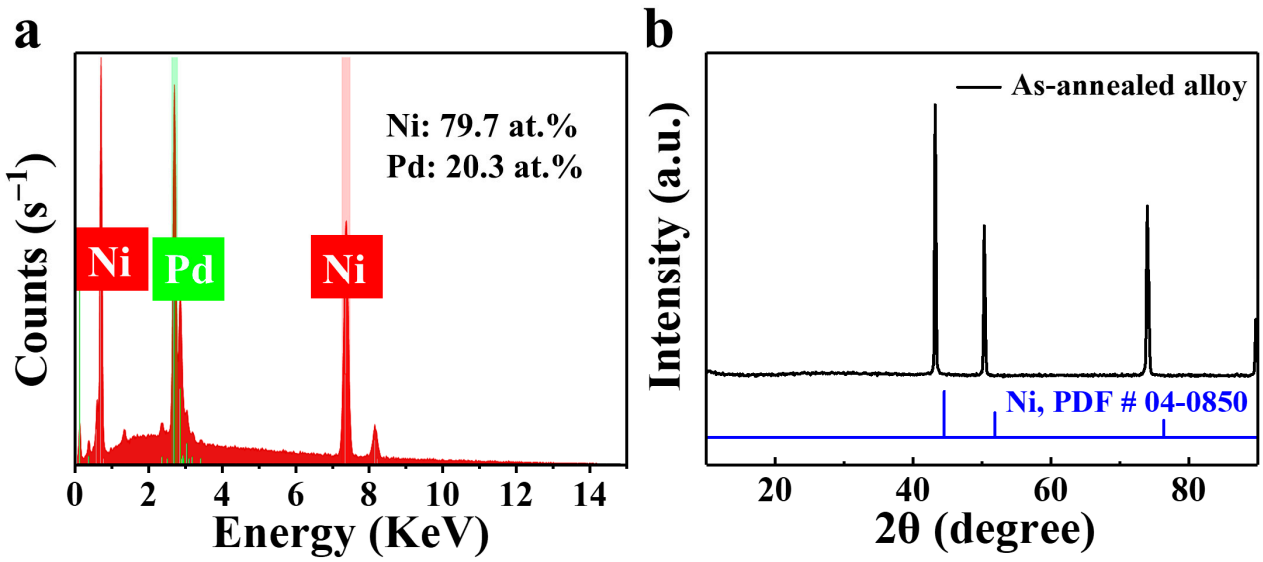

Figure 2. (**a**) Typical EDS spectrum and the average chemical compositions (inset) of the as-annealed $Ni_{80}Pd_{20}$ alloy. (**b**) XRD pattern of the as-annealed $Ni_{80}Pd_{20}$ alloy.

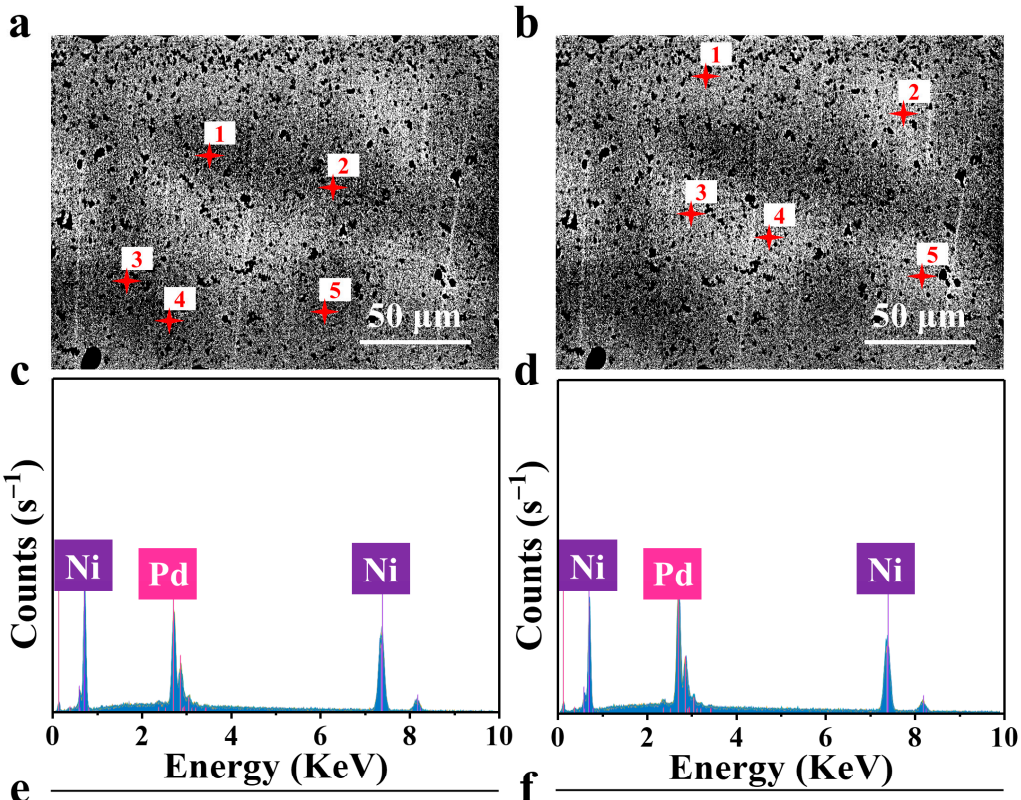

e

Site	Ni (at.%)	Pd (at.%)
1	79.8	20.2
2	80.1	19.9
3	79.8	20.2
4	81.0	19.0
5	79.9	20.1
Average value	80.1	19.9

f

Site	Ni (at.%)	Pd (at.%)
1	77.7	22.3
2	76.9	23.1
3	77.8	22.2
4	77.5	22.5
5	78.3	21.7
Average value	77.6	22.4

Figure 3. Spot-analysis results of the as-annealed $Ni_{80}Pd_{20}$ alloy for (**a**,**c**,**e**) the dark and (**b**,**d**,**f**) the grey regions, which correspond to two o solid–solution phases with extremely close chemical compositions, respectively.

To remove the Ni element, the as-annealed Ni–Pd alloy was dealloyed chemically. However, we found it difficult to completely remove Ni from the alloy whether HCl, H_2SO_4, or HNO_3 solution was used. As shown in Figure 4, the external surface of the samples still maintained a part of the metallic luster and retained a large amount of Ni (79.5 at.% for HCl, 70.1 at.% for H_2SO_4, and 45.2 at.% for HNO_3) even after 10 h of acid leaching. Simultaneously, no bubbles were detected on the surface of the samples during the leaching. In addition, the samples cannot be cut by a blade, implying that only the thin surface layer was dealloyed. Therefore, the as-annealed Ni–Pd alloy can be reasonably considered to possess chemical corrosion resistance even in strong acid solutions. Based on these results, we turned to the electrochemical dealloying method thanks to its salient advantages.

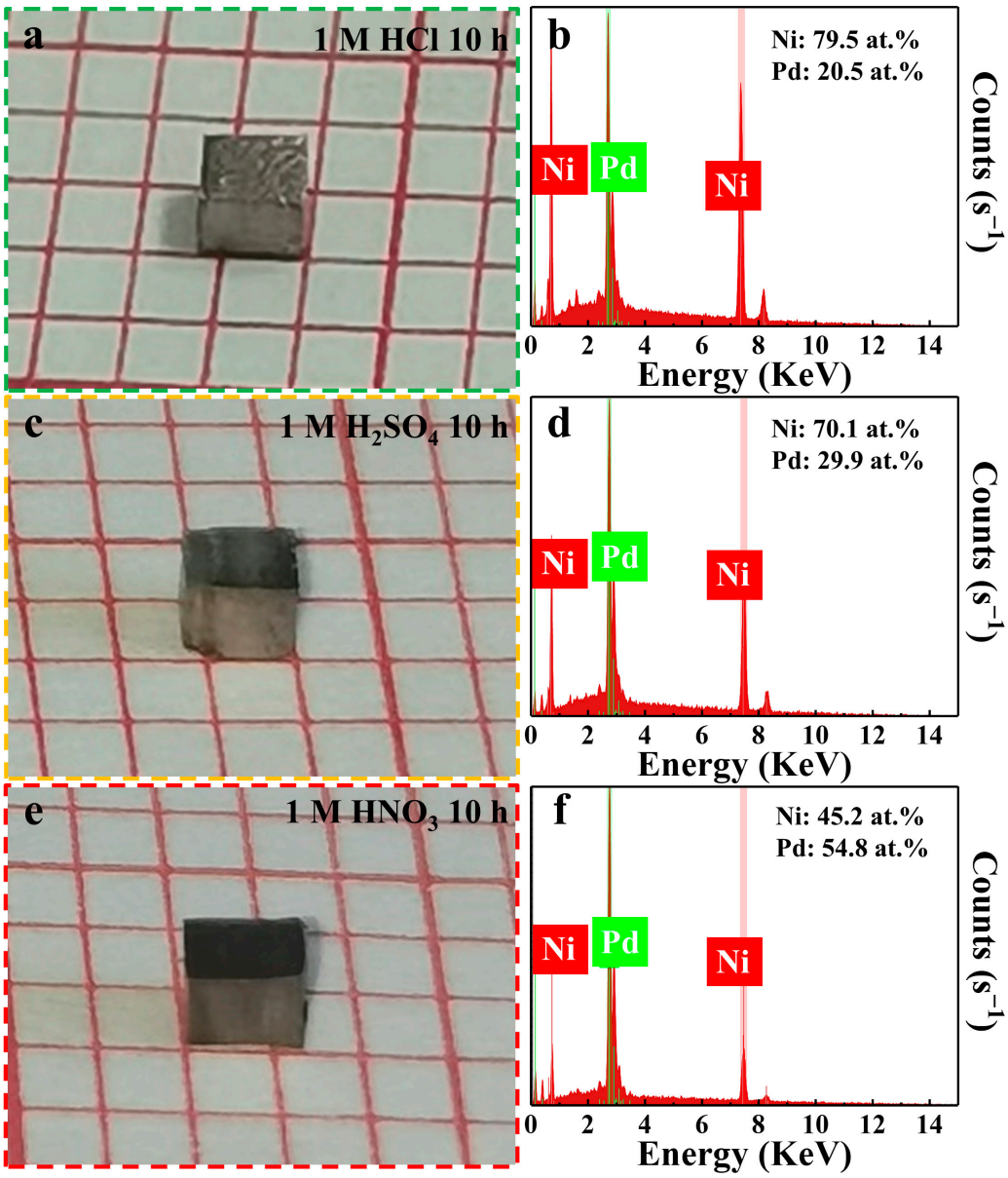

Figure 4. (**a**,**c**,**e**) The photos of the as-annealed $Ni_{80}Pd_{20}$ alloy after different acid leaching treatments, and (**b**,**d**,**f**) typical EDS spectra of the external surface of the corresponding samples. The average chemical compositions are shown in the EDS spectrum as an inset.

The corrosion potentials (E_{corr}) of the Ni, $Ni_{80}Pd_{20}$ and Pd were assessed in a 0.5 M H_2SO_4 solution, to determine the potential required to remove the active element (Ni) from the as-annealed alloy. Figure 5a shows the open-circuit potential (E_{ocp}) as a function of time. The horizontal line means that the electrode surface reached an equilibrium state. As expected, the equilibrium potential of the Ni is lower than that of the $Ni_{80}Pd_{20}$ alloy and Pd, indicating Ni possesses higher electrochemical activity in the 0.5 M H_2SO_4 solution [34]. The significant equilibrium potential difference between the components of the alloy is a prerequisite for electrochemical dealloying [35]. The polarization (Tafel) curves (Figure 5b) served to further confirm the electrochemical activity of the Ni, $Ni_{80}Pd_{20}$ and Pd. The corrosion current density (j_{corr}) and corrosion potential were determined by Tafel extrapolation (as shown in Figure 5b), and the results are presented in Table 1. As expected, the corrosion current densities of Ni and $Ni_{80}Pd_{20}$ are significantly higher that of Pd due to their different electrochemical activity in 0.5 M H_2SO_4. The potentials (E_{ocp}, E_{corr}) are slightly different, which is related to the surface state of the metals and the potential

scan rate [28,36]. Note that the corrosion potential of the as-annealed alloy deviates far from that of Ni and is close to that of Pd. The low electrochemical activity (high corrosion potential) further emphasizes the corrosion-resistance characteristic of the $Ni_{80}Pd_{20}$ alloy. Moreover, the polarization curves (Figure 5b) show that the maximum value of current density of Pd is relatively small after the applied potential exceeds its corrosion potential, meaning that Pd is stable in the electrochemical condition (0.5 M H_2SO_4).

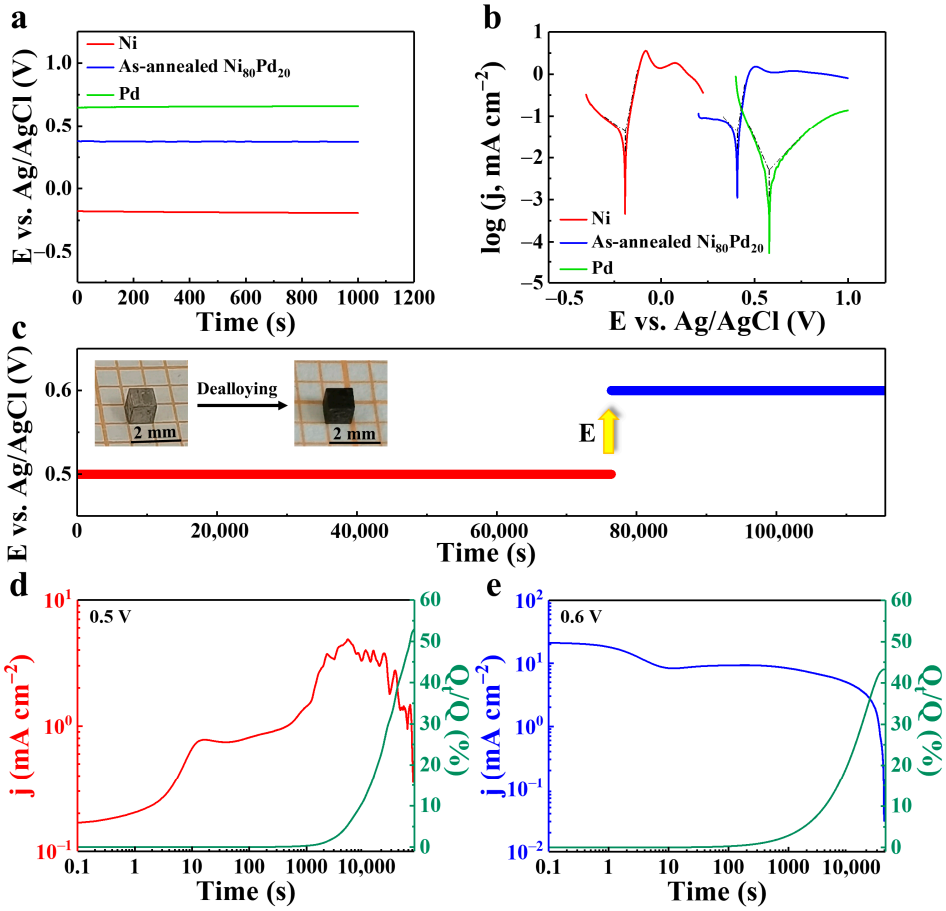

Figure 5. (**a**) Open-circuit potentials of Ni, $Ni_{80}Pd_{20}$ and Pd versus time. (**b**) Polarization plots of the Ni, $Ni_{80}Pd_{20}$, and Pd at the scan rate of 1 mV s^{-1}. (**c**) Dealloying potential versus time, and the insets present the photos of the as-annealed alloy and bulk np-Pd. The variation of current density (j) and charge ratio (Q_t/Q) with respect to time during (**d**) the first-step and (**e**) the second-step dealloying.

Table 1. The electrochemical activities of the Ni, $Ni_{80}Pd_{20}$ and Pd in the 0.5 M H_2SO_4 solution.

Metal	Open-Circuit Potential (E_{ocp} vs. Ag/AgCl)	Corrosion Potential (E_{corr} vs. Ag/AgCl)	Corrosion Current Density (j_{corr}, mA cm^{-2})
Ni	−0.18	−0.19	0.043
As-annealed $Ni_{80}Pd_{20}$	0.37	0.41	0.042
Pd	0.65	0.58	0.005

We firstly applied a potential of 0.5 V vs. Ag/AgCl to the $Ni_{80}Pd_{20}$ alloy until the current fell abruptly and approached zero. As a result, the cross-sectional EDS element analysis (Figure 6) shows that although the Ni in the region near the external surface of the as-dealloyed sample had been almost removed, a large amount of Ni (~62.4 at.%) remained in the sample center. This indicated that the corrosion rate had dropped to zero before completely removing Ni, which can be interpreted as the enrichment of Pd at the pore edges [37], and the increase in mass transport resistance during dealloying hinders the dissolution of Ni. To further remove Ni, the dealloying potential was subsequently

increased to 0.6 V vs. Ag/AgCl after the end of the first-step dealloying (Figure 5c). The transformation in the macroscopic morphology of the bulk sample before and after dealloying is shown as insets in Figure 5c.

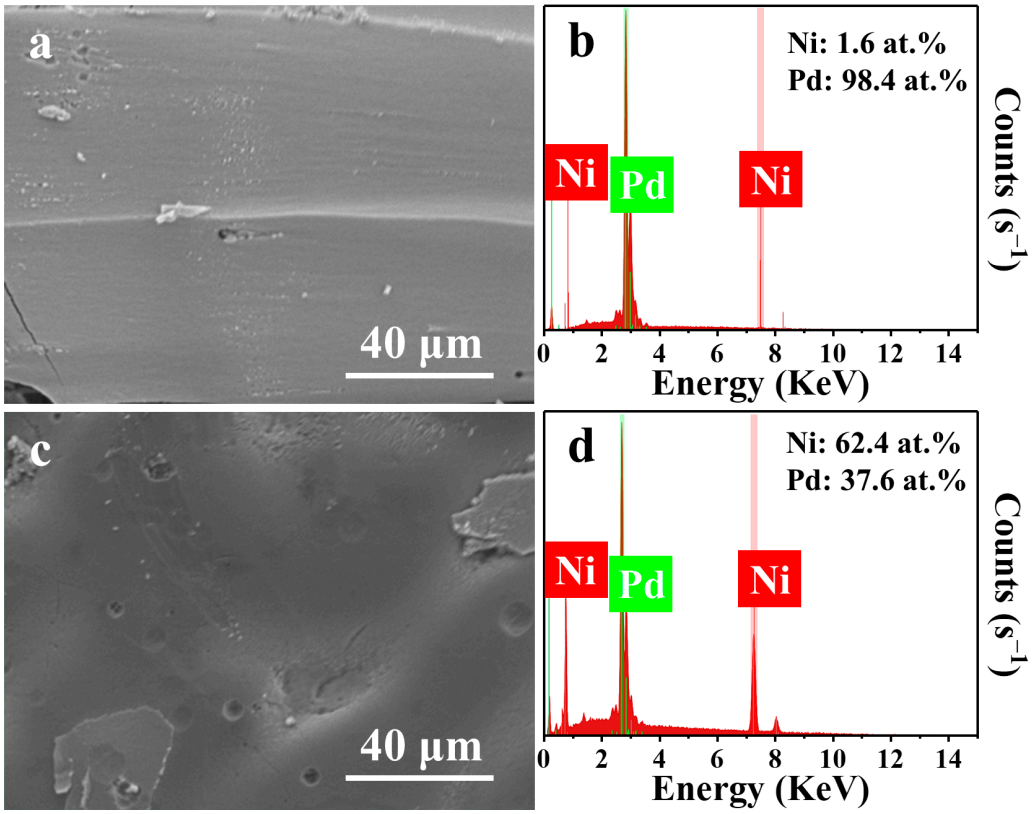

Figure 6. The SEM images and corresponding EDS spectra of (**a**,**b**) the region near the external surface and (**c**,**d**) the center of the sample after dealloying at 0.5 V vs. Ag/AgCl. The average chemical compositions are shown in the corresponding EDS spectrum as an inset.

Figure 5d,e shows the variation of j and charge ratio (Q_t/Q) versus the dealloying time. Q_t is the transferred charge obtained from the integration of current curves at the corresponding dealloying potential. The total amount of charges (Q) required to remove Ni altogether is based on the assumption that the total current originates from metallic Ni, which is oxidized to Ni^{2+}. Therefore, Q_t/Q represents the degree of dealloying [38,39]. During the first-step dealloying (Figure 5d), the current density increases to a peak after ~5000 s. Subsequently, a visible current density oscillation occurs, which can be explained by the passivation/activation of the surface resulting from the repeated formation/dissolution of the passivating film (especially for the Ni/H_2SO_4 system) [40–42]. When the oxide film is formed, the passivation of the surface leads to a decrease in current density. Since low current density is not conducive to the film formation, the rate of the film formation gradually becomes lower than its dissolution, thereby more active sites are exposed (activation of the surface), resulting in the current density rising, which prompts the film formation to start again, and the cycle repeats itself [40–42]. Eventually, the enrichment of Pd on the pore edges resulting from the removal of a large amount of Ni [37] and the mass transport resistance originating from increasingly curved nano-sized channels during dealloying lead to the cessation of corrosion. Subsequently, we applied a higher dealloying potential (0.6 V vs. Ag/AgCl) to further remove Ni. Due to the high potential during the second-step dealloying (Figure 5e), the electrode surface is activated and the corrosion process proceeds rapidly (higher current density than that of the first-step dealloying). Finally, the current density falls abruptly, and the sum of Q_t/Q of the two dealloying stages is close to 100%, implying that Ni has been almost completely removed. Moreover, the cross-sectional SEM

image (Figure 7) presents no un-dealloyed solid regions in the sample, and the EDS results (Figure 8) indicate that the content of Ni was reduced to <2 at.%, which again confirms the complete dealloying of the as-annealed Ni–Pd alloy.

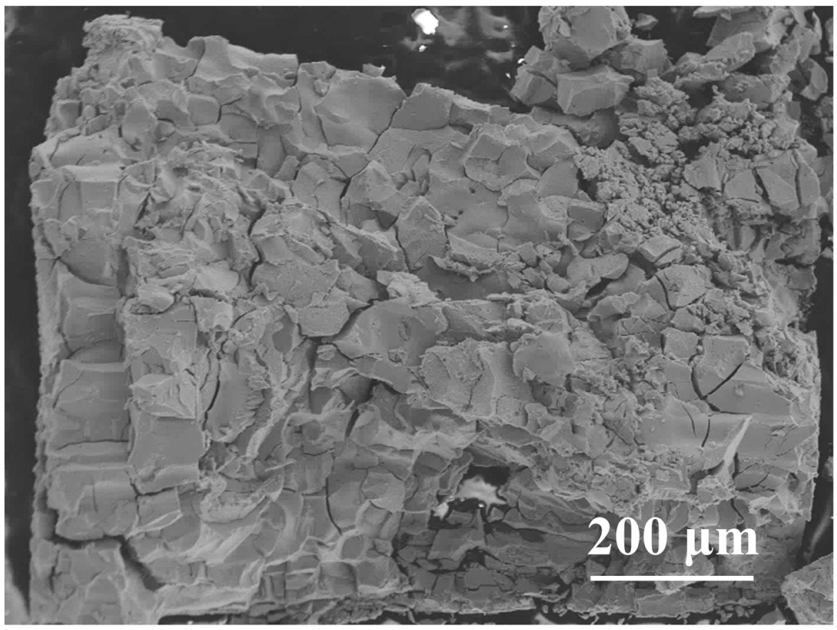

Figure 7. The cross-sectional SEM image of the bulk np-Pd fabricated by the two-step potentiostatic dealloying of $Ni_{80}Pd_{20}$.

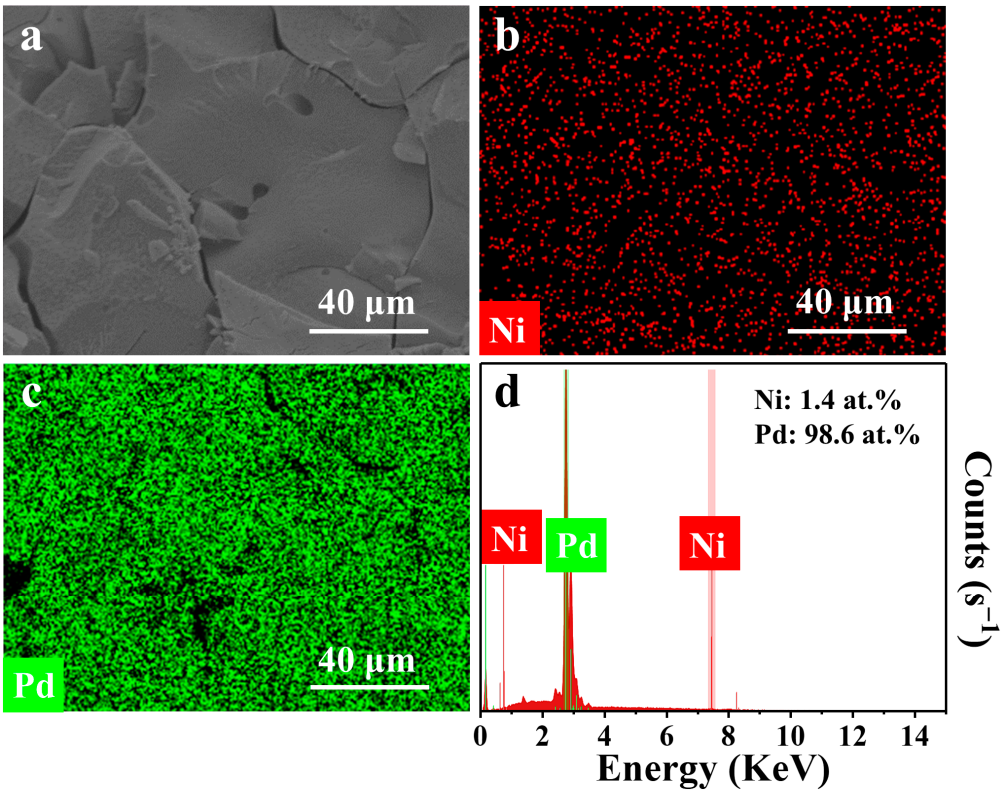

Figure 8. (**a**) Low-magnification SEM image and (**b**,**c**) the elemental distribution mappings of the bulk np-Pd fabricated by the two-step potentiostatic dealloying of $Ni_{80}Pd_{20}$. (**d**) The EDS spectrum of the bulk np-Pd, and the average residual amount of Ni is 1.4 at.%.

Consistent with the EDS results (Figure 8), the XRD pattern (Figure 9a) of the np-Pd reveals that only one set of diffraction peaks attributed to the fcc Pd phase (PDF # 46-1043) can be indexed. After the two-step potentiostatic dealloying, the cross-sectional SEM images of the bulk np-Pd (Figure 9b,c) present a uniform rather than hierarchical nanoporous structure with a ligament size of ~22 nm (inset in Figure 9c). The densely continuous nano-sized ligaments will provide good network connectivity for inducing strains [12,22]. The TEM images (Figure 9d,e) further reveal the dense nanoporous structure of the np-Pd. The black ligaments and bright nanopores are intertwined to form the interconnected ligament-channel network. In addition, the plane spacing (2.284 Å) in the high-resolution TEM (HRTEM) image (Figure 9f) is in accordance with the (111) crystal plane (2.246 Å) of the fcc Pd phase, and the selected-area electron diffraction (SAED) pattern (inset of Figure 9f) shows a series of visible polycrystalline rings, which can be indexed as (111), (200), (220) and (311) reflections of fcc Pd. These results demonstrate that the bulk np-Pd with a uniform and dense nanoporous structure was successfully fabricated by the two-step potentiostatic dealloying.

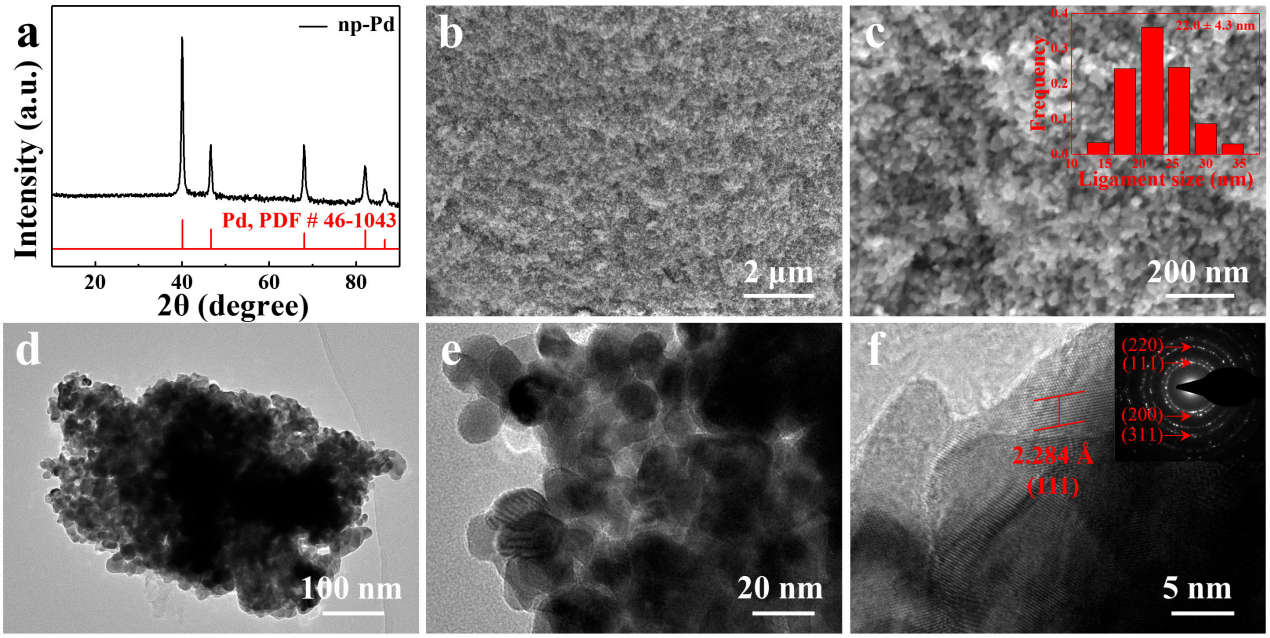

Figure 9. (**a**) XRD pattern, (**b**,**c**) SEM images, (**d**,**e**) TEM images, (**f**) HRTEM image and SAED pattern (inset) of the np-Pd. The ligament size distribution of the np-Pd is displayed in (**c**) as an inset.

Next, we investigated the electrochemical actuation behavior of the bulk np-Pd. The cyclic voltammetry (CV) technique was first employed. A series of periodically varying electrode potentials at different scan rates were applied to induce strains. Figure 10a records the cyclical actuation response at different scan rates from 50 to 1 mV s^{-1}, and the strain-time curves for high scan rates (from 50 to 10 mV s^{-1}) are magnified as an inset. Figure 10b shows the CV curve of the np-Pd at the scan rate of 1 mV s^{-1}. The forward potential scan from −1.4 to 1 V vs. SCE sequentially triggers the hydrogen adsorption/absorption (HA) (accompanied by hydrogen evolution [43]), hydrogen desorption (HD), OH adsorption (OA) and the formation of Pd oxides [16,44,45]. During the back scan, both the reduction of Pd oxides and OH desorption (OD) are proceeded.

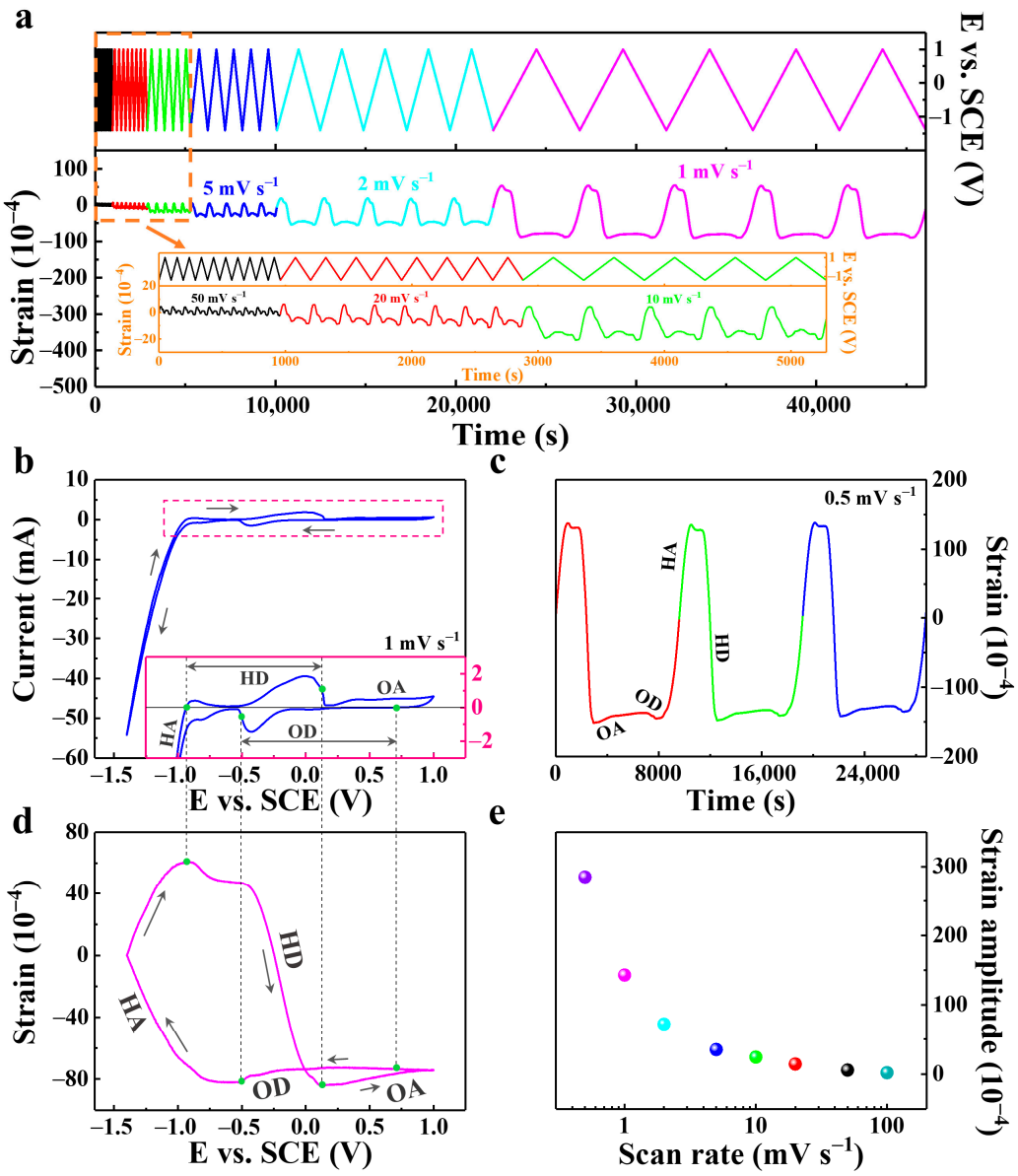

Figure 10. (**a**) CV-induced strain of the bulk np-Pd in 0.7 M NaF at different scan rates from 50 to 1 mV s^{-1}. (**b**) CV curve at the scan rate of 1 mV s^{-1} and an enlarge region for displaying details. (**c**) Successive strain response at the scan rate of 0.5 mV s^{-1}. (**d**) Strain as a function of the applied potential at the scan rate of 1 mV s^{-1}. (**e**) Strain amplitude versus the scan rate.

Figure 10c shows the strain-time curves with three continuous cycles at the scan rate of 0.5 mV s^{-1}, the electrochemical behaviors (HA, HD, OA and OD) corresponding to expansion and contraction are indicated in the curves. Combined with Figure 10b,d, the correspondence between the strain response and adsorption (absorption)/desorption behaviors of the species involved in the CV process can be clearly discerned. As the potential scan rate decreases (Figure 10e), more time is available for hydrogen adsorption/absorption, which induces larger lattice expansion and thus obtains more significant strain amplitudes [17]. Notably, the strain amplitude of np-Pd remarkably exceeds that of the reported np-Pd with coexisting micro- and nano-sized pores at the same scan rate [16]. Significantly, the amplitude is as high as 2.84% at the scan rate of 0.5 mV s^{-1}, which is close to the maximum strain amplitude (ε_{max} = 3.28%) of the reported np-Pd [16]. This demonstrates the advantages of the bulk np-Pd with a non-hierarchical and densely continuous network structure.

The square wave voltammetry (SWV) technique was used to determine the ε_{max} of the bulk np-Pd. Figure 11a records the SWV-induced strain response at a different applied potential time (period, t), and an enlarged region is shown in Figure 11b to see details at $t \leq 200$ s. Hydrogen desorption and adsorption/absorption occur repeatedly as the potential is frequently switched between 0.3 and −1.4 V vs. SCE, which induces reproducible contraction and expansion behaviors. The strain amplitudes can be well regulated by changing t. To know the ε_{max} of the bulk np-Pd, the $t/2$ is gradually extended to 10,000 s (Figure 11c), at which time the peak-to-peak strain amplitude is almost the same as that at $t/2$ = 5000 s. Thus, the ε_{max} was determined to be 3.74%. Such an amplitude outperforms that (3.28%) of the reported np-Pd with coexisting micro- and nano-sized pores [16] and close to that (4%) of the np-Pd with two nano-sized ligaments [17].

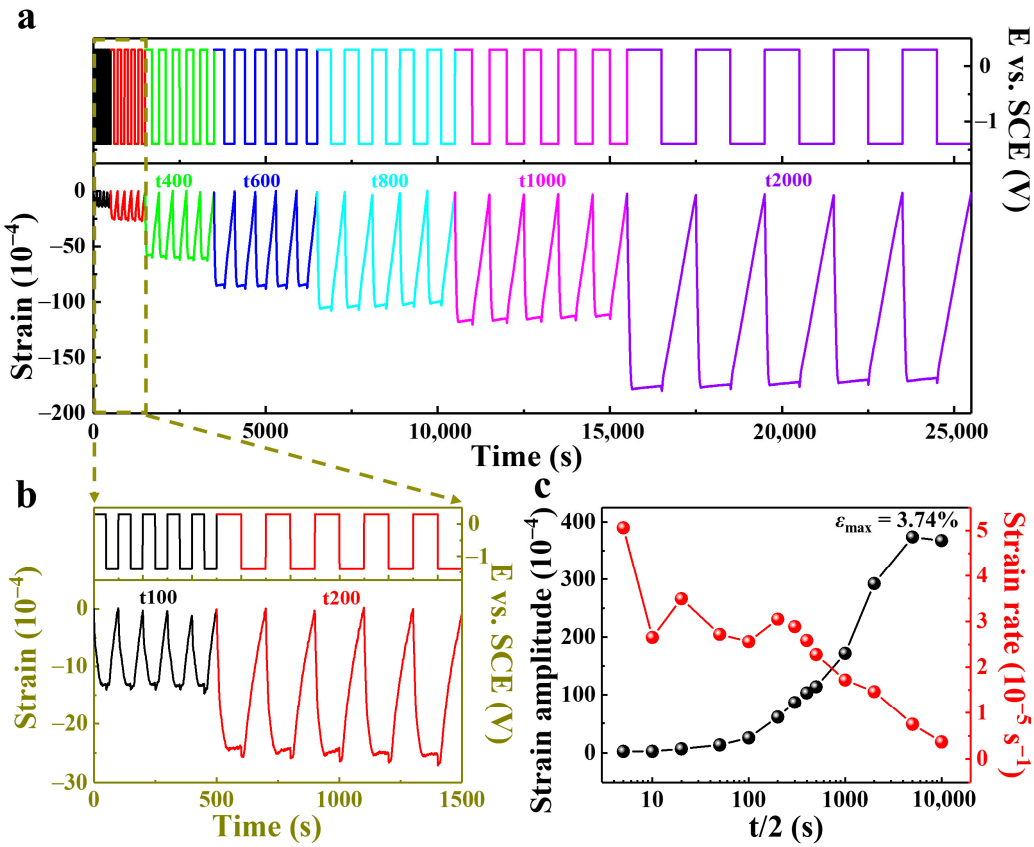

Figure 11. (**a**) SWV-induced strain response of the bulk np-Pd in 0.7 M NaF at different periods from 100 to 2000 s. (**b**) An enlarged region from (**a**). (**c**) Strain amplitude versus $t/2$.

In addition, the strain rate is a critical parameter for evaluating the actuation performance of bulk electrochemical metallic actuators, representing the average change in strain per unit time [46]. The hierarchically porous structure generally provides an efficient ion transport pathway [20,47], enabling fast strain rates. However, as presented in Figure 11c, the strain rate of our np-Pd with the non-hierarchical structure reaches the same order of magnitude as that (~10^{-5} s^{-1}) of the hierarchical np-Pd [16], and is much superior to those of np-Cu [18] and the consolidated np-Pt [10]. Furthermore, when the maximum strain amplitude is induced, the strain rate (7.48×10^{-6} s^{-1}) of our np-Pd is comparable to that (8.83×10^{-6} s^{-1}) of np-Ni with a semiordered hierarchical structure [14]. We consider that the large strain response is related to the network connectivity. As shown in Figure 9b,c, the bulk np-Pd possesses a dense nanoporous structure, these tightly intertwined ligaments provide a large number of interconnected bridges and thus establish good network connectivity, effectively contributing to the generation of overall actuation [12,22].

The strain energy density was also investigated further to assess the actuation performance of the bulk np-Pd. It is well known that the actuator can be considered a linear elastic solid [7,13,16,20]. Thus, the volume-specific strain energy density (w_V) was calculated by

$$w_V = ½\, Y_{eff}\, \varepsilon_{max}^2 \quad (1)$$

where Y_{eff} is the effective macroscopic Young's modulus [7,9] and can be obtained by regarding the as-dealloyed sample as an open-cell foam material via the following equation [48]:

$$Y_{eff} = Y_s\, (\rho_{np}/\rho_s)^2 \quad (2)$$

where Y_s (=121 GPa) is Young's modulus of solid Pd [16], and the ρ_{np} (=2.97 g cm^{-3}) and ρ_s (=12.023 g cm^{-3} [49]) are the densities of the bulk np-Pd and solid Pd, respectively. Thereby, the relative density (ρ_{np}/ρ_s) was determined to be 0.247 in this work. In addition, we can further attain the mass-specific strain energy density (w_M) using the equation:

$$w_M = w_V/\rho \quad (3)$$

where ρ is the mass density of the actuator material [7,9]. Therefore, Y_{eff}, w_V and w_M were calculated as 7.38 GPa, 5161 kJ m^{-3} (linear value), and 1738 J kg^{-1} (linear value), respectively.

We compare these parameters (Y_{eff}, ε_{max}, w_V, w_M) of the np-Pd with those of different actuator materials. Figure 12 shows the histogram of the performance comparisons (the data from Table 2). Significantly, our np-Pd not only possesses a higher ε_{max} than those of many actuator materials, such as piezoceramic [50], np-Ni [13] and np-AlNiCu [20], but also guarantees a moderate Y_{eff}. More importantly, the w_V and w_M of our np-Pd is at the highest level compared to those of typical actuator materials shown in Figure 12. In particular, the w_V and w_M of our np-Pd are 2.6 and 4.3 times as high as those of np-AuPt [7], respectively. Our results indicate that the bulk np-Pd with uniform and dense nanoporous structure possesses excellent comprehensive actuation performance.

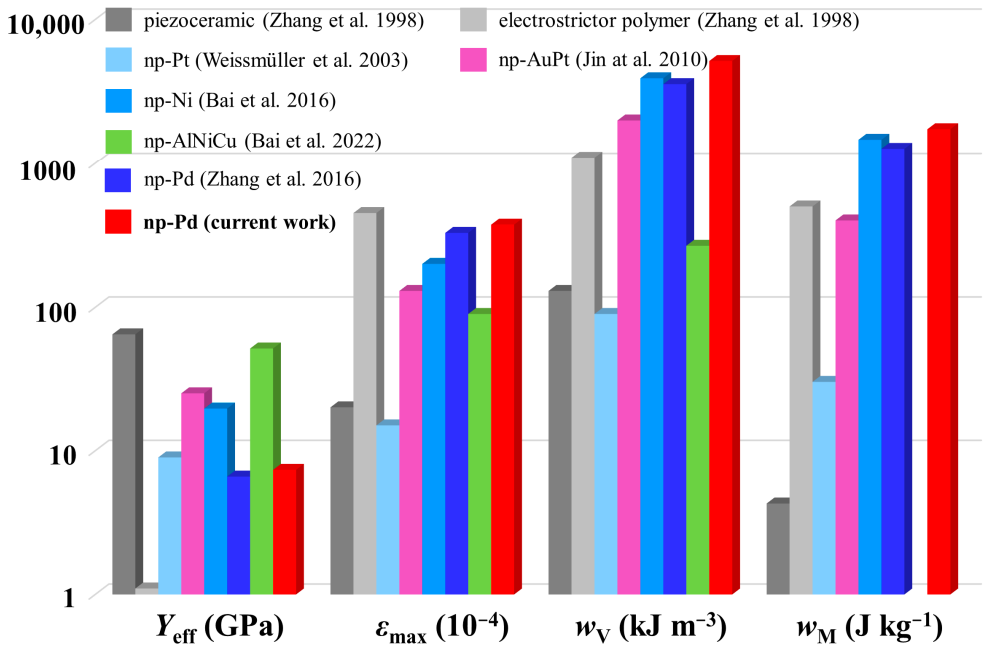

Figure 12. Comparisons of electrochemical actuation performance of various actuator materials [7,9,10,13,16,20,50].

Table 2. Figures of merit for various actuator materials.

Materials	Y_{eff} (GPa)	ε_{max} (10^{-4})	w_V (kJ m^{-3})	w_M (J kg^{-1})
piezoceramic [50]	64	20	130	4.25
electrostrictor polymer [50]	1.1	450	1100	500
np-Pt [9,10]	9	15	90	30
np-Au [12]	—	10	—	—
np-AuPt [7]	25	130	2000	400
np-Ni [13]	19.6	200	3920	1468
np-NiMn [15]	—	194	—	—
np-NiPd [51]	—	47	—	—
np-Pd [16]	6.63	328	3570	1270
np-Pd [17]	—	400	—	—
np-AlNiCu [20]	51.1	90	267	—
np-Pd (current work)	**7.38**	**374**	**5161**	**1738**

4. Conclusions

We successfully obtained the bulk np-Pd by the two-step potentiostatic dealloying of the as-annealed $Ni_{80}Pd_{20}$ alloy with chemical corrosion resistance. During dealloying, the formation/dissolution of the passivating film is treated as an important reason for the current density oscillation. The bulk np-Pd shows a dense nanoporous structure, which builds a great structural condition (good network connectivity) for large strain response. Therefore, the present np-Pd exhibits a large strain amplitude of up to 3.74% and high volume- and mass-specific strain energy density, exceeding those of many actuator materials. To sum up, the bulk np-Pd with dense nanoporous structure achieves excellent comprehensive actuation performance. Our work provides a meaningful reference in pursuit of superior electrochemical actuation performance of metallic materials.

Author Contributions: F.T.: Investigation, Writing—original draft. B.Y.: Investigation. Q.B.: Formal analysis, Writing—review and editing. Z.Z.: Supervision, Writing—review and editing, Funding acquisition. All authors have read and agreed to the published version of the manuscript.

Funding: This research was funded by the National Natural Science Foundation of China [52001234 and 51871133], the Taishan Scholar Foundation of Shandong Province, and the key research and development program of Shandong Province (2021ZLGX01).

Data Availability Statement: The data and results reported in this work are available on request from the corresponding author.

Acknowledgments: We acknowledge the financial support from the National Natural Science Foundation of China, the Taishan Scholar Foundation of Shandong Province, and the key research and development program of Shandong Province.

Conflicts of Interest: The authors declare that they have no competing financial interest or personal relationship that could have appeared to influence the work reported in this paper.

References

1. Sang, Q.; Hao, S.; Han, J.; Ding, Y. Dealloyed nanoporous materials for electrochemical energy conversion and storage. *EnergyChem* **2022**, *4*, 100069. [CrossRef]
2. Liu, X.; Zhu, S.; Liang, Y.; Jiang, H.; Li, Z.; Wu, S.; Cui, Z. Self-standing nanoporous NiPd bimetallic electrocatalysts with ultra-low Pd loading for efficient hydrogen evolution reaction. *Electrochim. Acta* **2022**, *411*, 140077. [CrossRef]
3. Wang, Z.; Liu, P.; Han, J.; Cheng, C.; Ning, S.; Hirata, A.; Fujita, T.; Chen, M. Engineering the internal surfaces of three-dimensional nanoporous catalysts by surfactant-modified dealloying. *Nat. Commun.* **2017**, *8*, 1066. [CrossRef]
4. Jayathilaka, W.; Qi, K.; Qin, Y.; Chinnappan, A.; Serrano-Garcia, W.; Baskar, C.; Wang, H.; He, J.; Cui, S.; Thomas, S.W.; et al. Significance of nanomaterials in wearables: A review on wearable actuators and sensors. *Adv. Mater.* **2019**, *31*, 1805921. [CrossRef]
5. An, Y.; Tian, Y.; Wei, C.; Tao, Y.; Xi, B.; Xiong, S.; Feng, J.; Qian, Y. Dealloying: An effective method for scalable fabrication of 0D, 1D, 2D, 3D materials and its application in energy storage. *Nano Today* **2021**, *37*, 101094. [CrossRef]
6. Jin, H.J.; Weissmüller, J. Bulk nanoporous metal for actuation. *Adv. Eng. Mater.* **2010**, *12*, 714–723. [CrossRef]
7. Jin, H.J.; Wang, X.L.; Parida, S.; Wang, K.; Seo, M.; Weissmüller, J. Nanoporous Au-Pt alloys as large strain electrochemical actuators. *Nano Lett.* **2010**, *10*, 187–194. [CrossRef]

8. Mirfakhrai, T.; Madden, J.D.W.; Baughman, R.H. Polymer artificial muscles. *Mater. Today* **2007**, *10*, 30–38. [CrossRef]
9. Weissmüller, J.; Viswanath, R.N.; Kramer, D.; Zimmer, P.; Würschum, R.; Gleiter, H. Charge-induced reversible strain in a metal. *Science* **2003**, *300*, 312–315. [CrossRef]
10. Viswanath, R.N.; Kramer, D.; Weissmüller, J. Adsorbate effects on the surface stress-charge response of platinum electrodes. *Electrochim. Acta* **2008**, *53*, 2757–2767. [CrossRef]
11. Jin, H.J.; Parida, S.; Kramer, D.; Weissmüller, J. Sign-inverted surface stress-charge response in nanoporous gold. *Surf. Sci.* **2008**, *602*, 3588–3594. [CrossRef]
12. Cheng, C.; Lührs, L. Robust metallic actuators based on nanoporous gold rapidly dealloyed from gold-nickel precursors. *Adv. Funct. Mater.* **2021**, *31*, 2107241. [CrossRef]
13. Bai, Q.; Wang, Y.; Zhang, J.; Ding, Y.; Peng, Z.; Zhang, Z. Hierarchically nanoporous nickel-based actuators with giant reversible strain and ultrahigh work density. *J. Mater. Chem. C* **2016**, *4*, 45–52. [CrossRef]
14. Cheng, C.; Lührs, L.; Krekeler, T.; Ritter, M.; Weissmüller, J. Semiordered hierarchical metallic network for fast and large charge-induced strain. *Nano Lett.* **2017**, *17*, 4774–4780. [CrossRef]
15. Cheng, C.; Lührs, L.; Krekeler, T. Simultaneous enhancement of actuation strain and mechanical strength of nanoporous Ni-Mn actuators. *Adv. Electron. Mater.* **2021**, *7*, 2100381. [CrossRef]
16. Zhang, J.; Bai, Q.; Zhang, Z. Dealloying-driven nanoporous palladium with superior electrochemical actuation performance. *Nanoscale* **2016**, *8*, 7287–7295. [CrossRef]
17. Shi, S.; Markmann, J.; Weissmüller, J. Actuation by hydrogen electrosorption in hierarchical nanoporous palladium. *Philos. Mag.* **2017**, *97*, 1571–1587. [CrossRef]
18. Bai, Q.; Zhang, C.; Tan, F.; Wu, F.; Zhang, Z. Nanoporous copper as an inexpensive electrochemical actuator responsive to sub-volt voltages. *Electrochem. Commun.* **2021**, *124*, 106940. [CrossRef]
19. Tan, F.; Yu, B.; Yan, X.; Zhang, Y.; Bai, Q.; Zhang, J.; Zhang, Z. Electrochemical actuation behaviors of bulk nanoporous copper with a hierarchical structure. *J. Alloys Compd.* **2022**, *923*, 166469. [CrossRef]
20. Bai, Q.; Zhang, C.; Tan, F.; Zhang, Z. High-performance, low-cost nanoporous alloy actuators by one-step dealloying of Al-Ni-Cu precursors. *Intermetallics* **2022**, *145*, 107537. [CrossRef]
21. Li, J.; Markmann, J.; Weissmüller, J.; Mameka, N. Nanoporous gold-polypyrrole hybrid electrochemical actuators with tunable elasticity. *Acta Mater.* **2021**, *212*, 116852. [CrossRef]
22. Roschning, B.; Weissmüller, J. Nanoporous-gold-polypyrrole hybrid materials for millimeter-sized free standing actuators. *Adv. Mater. Interfaces* **2020**, *7*, 2001415. [CrossRef]
23. Wang, K.; Stenner, C.; Weissmüller, J. A nanoporous gold-polypyrrole hybrid nanomaterial for actuation. *Sens. Actuators B Chem.* **2017**, *248*, 622–629. [CrossRef]
24. Detsi, E.; Onck, P.; De Hosson, J.T.M. Metallic muscles at work: High rate actuation in nanoporous gold/polyaniline composites. *ACS Nano* **2013**, *7*, 4299–4306. [CrossRef]
25. Liu, Y.; Bliznakov, S.; Dimitrov, N. Factors controlling the less noble metal retention in nanoporous structures processed by electrochemical dealloying. *J. Electrochem. Soc.* **2010**, *157*, K168–K176. [CrossRef]
26. Li, Y.; Ngo-Dinh, B.-N.; Markmann, J.; Weissmüller, J. Evolution of length scales and of chemical heterogeneity during primary and secondary dealloying. *Acta Mater.* **2022**, *222*, 117424. [CrossRef]
27. Rurainsky, C.; Manjón, A.G.; Hiege, F.; Chen, Y.-T.; Scheu, C.; Tschulik, K. Electrochemical dealloying as a tool to tune the porosity, composition and catalytic activity of nanomaterials. *J. Mater. Chem. A* **2020**, *8*, 19405–19413. [CrossRef]
28. Zhang, Q.; Zhang, Z. On the electrochemical dealloying of Al-based alloys in a NaCl aqueous solution. *Phys. Chem. Chem. Phys.* **2010**, *12*, 1453–1472. [CrossRef]
29. Palcut, M.; Ďuriška, L.; Špoták, M.; Vrbovský, M.; Gerhátová, Ž.; Černičková, I.; Janovec, J. Electrochemical corrosion of Al-Pd alloys in HCl and NaOH solutions. *J. Min. Metall. Sect. B-Metall.* **2017**, *53*, 333–340. [CrossRef]
30. Shi, S.; Markmann, J.; Weissmüller, J. Synthesis of uniform bulk nanoporous palladium with tunable structure. *Electrochim. Acta* **2018**, *285*, 60–69. [CrossRef]
31. Sun, L.; Li, J.; Xu, R.; He, S.; Hua, Z.; Liu, H. One-step rapid synthesis of a 3D porous surface on Zr-based bulk metallic glass. *Surf. Coat. Technol.* **2021**, *418*, 127230. [CrossRef]
32. Xu, J.; Zhang, C.; Wang, X.; Ji, H.; Zhao, C.; Wang, Y.; Zhang, Z. Fabrication of bi-modal nanoporous bimetallic Pt-Au alloy with excellent electrocatalytic performance towards formic acid oxidation. *Green Chem.* **2011**, *13*, 1914–1922. [CrossRef]
33. Snyder, J.; Livi, K.; Erlebacher, J. Dealloying silver/gold alloys in neutral silver nitrate solution: Porosity evolution, surface composition, and surface oxides. *J. Electrochem. Soc.* **2008**, *155*, C464–C473. [CrossRef]
34. Li, M.; Liu, J.; Wang, C.; Liu, Y.; Sun, Y.; Qin, C.; Wang, Z.; Li, Y.; Liu, L.; Liu, S. Controllable nanoporous copper synthesized by dealloying metallic glasses: New insights into the tuning pore structure and applications. *Chem. Eng. J.* **2022**, *427*, 130861. [CrossRef]
35. Erlebacher, J. An atomistic description of dealloying porosity evolution, the critical potential, and rate-limiting behavior. *J. Electrochem. Soc.* **2004**, *151*, C614–C626. [CrossRef]
36. Sieradzki, K.; Dimitrov, N.; Movrin, D.; McCall, C.; Vasiljevic, N.; Erlebacher, J. The dealloying critical potential. *J. Electrochem. Soc.* **2002**, *149*, B370–B377. [CrossRef]

37. Damian, A.; Maroun, F.; Allongue, P. Electrochemical de-alloying in two dimensions: Role of the local atomic environment. *Nanoscale* **2016**, *8*, 13985–13996. [CrossRef]
38. Graf, M.; Roschning, B.; Weissmüller, J. Nanoporous gold by alloy corrosion: Method-structure-property relationships. *J. Electrochem. Soc.* **2017**, *164*, C194–C200. [CrossRef]
39. Wittstock, A.; Zielasek, V.; Biener, J.; Friend, C.M.; Baumer, M. Nanoporous gold catalysts for selective gas-phase oxidative coupling of methanol at low temperature. *Science* **2010**, *327*, 319–322. [CrossRef]
40. dos Santos, C.G.P.; Machado, E.G.; Kiss, I.Z.; Nagao, R. Investigation of the oscillatory electrodissolution of the Nickel-Iron alloy. *J. Phys. Chem. C* **2019**, *123*, 24087–24094. [CrossRef]
41. Hudson, J.L.; Tsotsis, T.T. Electrochemical reaction dynamics: A review. *Chem. Eng. Sci.* **1994**, *49*, 1493–1572. [CrossRef]
42. Schmuki, P. From Bacon to barriers: A review on the passivity of metals and alloys. *J. Solid State Electrochem.* **2002**, *6*, 145–164. [CrossRef]
43. Czerwiński, A.; Kiersztyn, I.; Grdeń, M. The study of hydrogen sorption in palladium limited volume electrodes (Pd-LVE): Part II. Basic solutions. *J. Electroanal. Chem.* **2000**, *492*, 128–136. [CrossRef]
44. Pan, W.; Zhang, X.; Ma, H.; Zhang, J. Electrochemical synthesis, voltammetric behavior, and electrocatalytic activity of Pd nanoparticles. *J. Phys. Chem. C* **2008**, *112*, 2456–2461. [CrossRef]
45. Grdeń, M.; Łukaszewski, M.; Jerkiewicz, G.; Czerwiński, A. Electrochemical behaviour of palladium electrode: Oxidation, electrodissolution and ionic adsorption. *Electrochim. Acta* **2008**, *53*, 7583–7598. [CrossRef]
46. Madden, J.D.W.; Vandesteeg, N.A.; Anquetil, P.A.; Madden, P.G.A.; Takshi, A.; Pytel, R.Z.; Lafontaine, S.R.; Wieringa, P.A.; Hunter, I.W. Artificial muscle technology: Physical principles and naval prospects. *IEEE J. Ocean. Eng.* **2004**, *29*, 706–728. [CrossRef]
47. Juarez, T.; Biener, J.; Weissmüller, J.; Hodge, A.M. Nanoporous metals with structural hierarchy: A review. *Adv. Eng. Mater.* **2017**, *19*, 1700389. [CrossRef]
48. Biener, J.; Hodge, A.M.; Hamza, A.V.; Hsiung, L.M.; Satcher, J.H., Jr. Nanoporous Au: A high yield strength material. *J. Appl. Phys.* **2005**, *97*, 024301. [CrossRef]
49. Viswanath, R.N.; Weissmüller, J. Electrocapillary coupling coefficients for hydrogen electrosorption on palladium. *Acta Mater.* **2013**, *61*, 6301–6309. [CrossRef]
50. Zhang, Q.M.; Bharti, V.; Zhao, X. Giant electrostriction and relaxor ferroelectric behavior in electron-irradiated poly(vinylidene fluoride-trifluoroethylene) copolymer. *Science* **1998**, *280*, 2101–2104. [CrossRef]
51. Zhang, J.; Lv, L.; Gao, H.; Bai, Q.; Zhang, C.; Zhang, Z. Electrochemical actuation behaviors and mechanisms of bulk nanoporous Ni-Pd alloy. *Scr. Mater.* **2017**, *137*, 73–77. [CrossRef]